Uniosun Journal of Engineering and Environmental Sciences (UJEES), Vol. 8 No. 2, Sept., 2026
DOI: 10.64980/ujees.v8i2.033 **Adejo et al.**
Published: September 30, 2026

MACHINE LEARNING-BASED PREDICTION AND ANALYSIS OF ATMOSPHERIC REFRACTIVITY (N-UNIT) PROFILES OVER IKEJA, NIGERIA: A COMPREHENSIVE STUDY WITH IMPLICATIONS FOR RADIO WAVE PROPAGATION

O. ADEJO[1], M. K. BAMGBOSE[2*], L. B. KOLAWOLE[3]

[1,2]*Department of Physics, Lagos State University Ojo, PMB 001, Ojo, Lagos State, Nigeria*

[3]*Department of Physics, Redeemer's University Ede, Osun State, Nigeria*

[*]*Corresponding Author: muyiwa.bamgbose@lasu.edu.ng*

Abstract
Atmospheric refractivity (N-unit) is a critical parameter in radio wave propagation and communication systems design. This study presents a comprehensive analysis of atmospheric refractivity profiles using machine learning techniques, based on high-resolution data collected at Ikeja, Nigeria (6.60° N, 3.35° E) during January 2020. Measurements were taken at seven different heights ranging from 2 m to 1237 m above ground level at hourly intervals, providing 744 observations per height level. We employed ten different regression algorithms, including Linear Regression, Ridge, Lasso, Elastic Net, Decision Tree, Random Forest, Gradient Boosting, AdaBoost, K-Nearest Neighbors, and Support Vector Regression to model and predict N-unit values at near-surface level (2 m). Time-based features (hour, day) were transformed using cyclical encoding, and lag features alongside rolling statistics were engineered to capture temporal dependencies. Results indicate that ensemble methods significantly outperform linear models, with Gradient Boosting achieving the highest prediction accuracy (R^2 = 0.94, RMSE = 5.23, MAE = 3.87, MAPE = 1.24%). Feature importance analysis revealed that lag features (particularly 6-hour and 12-hour lags) and rolling statistics are the most influential predictors, highlighting the strong temporal autocorrelation in atmospheric refractivity. Vertical profile analysis showed decreasing correlation with height (from 0.89 at 111 m to 0.31 at 1237 m relative to surface measurements) following an exponential decay model $r(h) = 0.92 \times \exp(-h/850)$. Maximum variability was observed at 325 m (CV = 15.7%), likely associated with the boundary layer entrainment zone. Time series cross-validation confirmed model robustness with mean R^2 = 0.93 ± 0.02. This study demonstrates the efficacy of machine learning approaches for atmospheric refractivity prediction and provides valuable insights for radio propagation modeling in tropical regions, while carefully accounting for single-season and single-station dataset constraints.

Keywords
Atmospheric refractivity, N-unit, machine learning, radio wave propagation, tropical atmosphere, Ikeja, boundary layer, ensemble methods, time series analysis

1. INTRODUCTION

Atmospheric refractivity, commonly expressed in N-units, is a fundamental parameter in radio wave propagation studies. It describes the bending of electromagnetic waves as they travel through the atmosphere due to spatial variations in refractive index [1, 2]. The N-unit is defined by the equation:

$$N = (n - 1) \times 10^6 \quad (1)$$

where N represents the atmospheric refractivity in N-units, and n is the refractive index of air. Accurate knowledge of atmospheric refractivity profiles is essential for various applications, including radio communication link design, radar performance assessment, and weather forecasting [3, 4, 5, 6].

The atmospheric boundary layer exhibits complex temporal and spatial variations in refractivity, particularly in tropical regions where diurnal cycles and convective activities significantly influence atmospheric structure [7, 8, 9, 10]. Nigeria, located in West Africa between latitudes 4° N and 14° N, experiences distinct wet and dry seasons with corresponding variations in temperature, pressure, and humidity - the primary meteorological parameters affecting refractivity [11, 12, 13, 14].

Recent years have witnessed significant advancements in atmospheric refractivity research, particularly with the integration of machine learning techniques. [14] applied deep learning methods to predict radio refractivity gradients over West Africa using ERA5 reanalysis data, achieving unprecedented accuracy in capturing spatial-temporal variations. [10] conducted a comprehensive analysis of long-term trends in atmospheric refractivity over Nigeria from 1980 to 2025, revealing significant climate-induced changes in vertical profiles.

The application of explainable artificial intelligence (XAI) to atmospheric science has gained momentum, with [15] developing interpretable models for refractivity prediction in tropical environments. Their work demonstrated that feature importance analysis can provide physical insights while maintaining high predictive accuracy. Similarly, recent machine learning forecasting studies [16] have shown that data-driven approaches can achieve strong predictive skill at reduced computational cost compared with some traditional numerical workflows. [17] explored artificial intelligence techniques for predicting atmospheric radio ducts in tropical regions, identifying critical parameters that lead to anomalous propagation conditions.

The integration of ground-based measurements with satellite observations has opened new avenues for refractivity research. [18] developed transformer-based deep learning models for retrieving aerosol optical properties from multi-angle polarimetric satellite observations, while [19] focused on radiometric monitoring of directional polarimetric cameras using ice clouds as calibration targets. [20] applied the GRASP (Generalized Retrieval of Aerosol and Surface Properties) algorithm with multi-angle polarimetric measurements, demonstrating improved accuracy in aerosol characterization.

Ikeja (6.60° N, 3.35° E), the capital city of Lagos State, Nigeria, represents a unique urban tropical environment. Lagos is one of the fastest-growing megacities in Africa, with significant implications for communication infrastructure planning [21, 22]. The January period represents the dry season (harmattan), characterized by relatively low humidity, moderate temperatures, and Saharan dust influence [23, 24].

Building on these recent advances, this study aims to characterize the vertical and temporal variations of atmospheric refractivity over Ikeja, Nigeria, during January 2020. We seek to develop and compare multiple machine learning models for predicting near-surface (2 m) N-unit values, including state-of-the-art ensemble methods. Through comprehensive feature importance analysis, we aim to identify the most significant predictors of atmospheric refractivity. The study validates model performance using time series cross-validation techniques appropriate for atmospheric data and provides quantitative insights for radio propagation modeling in tropical urban environments.

The remainder of this paper is organized as follows: Section 2 describes the study area, data collection, preprocessing techniques, feature engineering, and machine learning methodology. Section 3 presents the exploratory data analysis, model performance comparison, feature importance analysis, and validation results. Section 4 interprets the findings in the context of atmospheric physics and practical applications, relating them to recent studies and outlining methodological limitations. Section 5 summarizes the key findings and suggests directions for future research.

2. MATERIALS AND METHOD

2.1 Study Area Description

The study was conducted at Ikeja (6.60° N, 3.35° E), the capital city of Lagos State in southwestern Nigeria. Lagos State is situated along the Gulf of Guinea and experiences a tropical monsoon climate (Köppen climate classification Am) with distinct wet (April-October) and dry (November-March) seasons [25]. January falls within the dry season, characterized by mean temperature ranges of 25-32 °C and mean relative humidity between 60 and 80 percent. The predominant wind direction is northeast, bringing harmattan winds with moderate to high Saharan dust influence. Average atmospheric pressure ranges from 1012 to 1015 hPa, while typical boundary layer heights reach 300 to 500 meters during daytime [26].

2.2 Data Collection

Data were collected throughout January 2020 (31 days) using radiosonde measurements at the Ikeja meteorological station. Measurements were recorded hourly at seven different heights above ground level. Table 1 presents the measurement heights and their corresponding atmospheric layers.

The dataset comprises 744 hourly observations (31 days multiplied by 24 hours) for each height level, providing a comprehensive temporal record suitable for time series analysis and machine learning applications [27, 28, 29].

2.3 Data Preprocessing

Initial data exploration revealed no missing values. The dataset was structured with columns for month (constant value of 1 representing January), day (1-31), hour (0-23), and N-unit measurements at each height. A datetime index was created combining day and hour information to facilitate time series analysis.

Table 1: Measurement heights and corresponding atmospheric layers.

Height (m)	Column Name	Atmospheric Layer
2	N-Unit (2m)	Surface layer
111	N-Unit (111m)	Lower boundary layer
325	N-Unit (325m)	Middle boundary layer
544	N-Unit (544m)	Upper boundary layer
769	N-Unit (769m)	Entrainment zone
1000	N-Unit (1000m)	Lower free troposphere
1237	N-Unit (1237m)	Free troposphere

2.4 Exploratory Data Analysis

A comprehensive exploratory analysis was performed to understand the data characteristics. Pearson correlation coefficients were calculated between all height levels to understand the vertical coupling of atmospheric refractivity. The correlation coefficient r_{xy} is defined as:

$$r_{xy} = \frac{\sum_{i=1}^{n}(x_i - \bar{x})(y_i - \bar{y})}{\sqrt{\sum_{i=1}^{n}(x_i - \bar{x})^2 \sum_{i=1}^{n}(y_i - \bar{y})^2}} \quad (2)$$

where x_i and y_i are individual observations at different heights, and $\bar{x}$ and $\bar{y}$ represent their respective mean values [1]. Hourly statistics, including mean, standard deviation, minimum, and maximum, were computed for each height to quantify diurnal variability, following the methodology of [21]. The coefficient of variation (CV_h) was calculated for each height to assess relative variability, defined as:

$$CV_h = \frac{\sigma_h}{\mu_h} \times 100\% \quad (3)$$

where σ_h is the standard deviation and μ_h is the mean at height h.

2.5 Feature Engineering

For machine learning prediction of near-surface N-unit values, with the target variable being N-Unit measured at 2 meters, we engineered several feature categories to capture temporal dependencies and patterns, building on approaches from [29] and [15].

Hour and day features were transformed using sine-cosine encoding to preserve cyclical continuity [28]:

$$\text{hour_sin} = \sin\left(\frac{2\pi \times \text{hour}}{24}\right) \quad (4)$$

$$\text{hour_cos} = \cos\left(\frac{2\pi \times \text{hour}}{24}\right) \quad (5)$$

$$\text{day_sin} = \sin\left(\frac{2\pi \times \text{day}}{31}\right) \quad (6)$$

$$\text{day_cos} = \cos\left(\frac{2\pi \times \text{day}}{31}\right) \quad (7)$$

This encoding ensures that hour 23 and hour 0 are treated as adjacent values, preserving the cyclical nature of time.

Additional temporal features were created to capture various temporal patterns. Day of week, ranging from 0 (Monday) to 6 (Sunday), captures weekly patterns in atmospheric conditions. A weekend indicator, taking the value 1 for Saturday and Sunday and 0 otherwise, accounts for potential anthropogenic effects. Time category segmentation divides the day into morning from 5 to 11 hours, afternoon from 12 to 16 hours, evening from 17 to 20 hours, and night from 21 to 4 hours.

To capture temporal autocorrelation, lag features were created for the target variable [27, 14]:

$$L_k(t) = y(t-k) \qquad \text{for} \quad k \in \{1,2,3,6,12,24\} \quad (8)$$

where $y(t)$ represents the N-unit value at time t. These specific lags were chosen based on partial autocorrelation function analysis and standard time-series practice [27, 30].

Moving window statistics were computed to capture local trends and variability [30, 31]:

$$\mathrm{MA}_w(t) = \frac{1}{w}\sum_{i=0}^{w-1} y(t-i) \tag{9}$$

$$\mathrm{SD}_w(t) = \sqrt{\frac{1}{w}\sum_{i=0}^{w-1} [y(t-i) - \mathrm{MA}_w(t)]^2} \tag{10}$$

for window sizes $w \in \{3,6,12,24\}$ hours, representing 3-hour, 6-hour, 12-hour, and 24-hour periods.

To ensure zero data leakage during machine learning model development, all feature engineering operations—including cyclical encoding, lag features, and rolling window statistics—were computed strictly using historical observations prior to or at time step *t*. Chronological data splitting was strictly enforced, allocating the first 80 percent of observations for training and the remaining 20 percent for testing.

2.6 Machine Learning Models

Ten regression algorithms were implemented and compared, representing different classes of machine learning approaches [32, 33, 34]. The linear models included Linear Regression as a baseline model, assuming a linear relationship between features and target, expressed as:

$$\hat{y} = \beta_0 + \sum_{j=1}^{p} \beta_j x_j \tag{11}$$

[35]. Ridge Regression applies linear regression with L2 regularization to prevent overfitting, where the beta coefficients minimize the sum of squared errors plus λ times the sum of squared beta coefficients [36]:

$$\hat{\beta} = \arg\min_{\beta} \left\{ \sum_{i=1}^{n} \left(y_i - \beta_0 - \sum_{j=1}^{p} \beta_j x_{ij} \right)^2 + \lambda \sum_{j=1}^{p} {\beta_j}^2 \right\} \tag{12}$$

where λ is the regularization hyperparameter. Lasso Regression employs linear regression with L1 regularization for feature selection, minimizing the sum of squared errors plus λ times the sum of absolute beta coefficients [37]:

$$\hat{\beta} = \arg\min_{\beta} \left\{ \sum_{i=1}^{n} \left(y_i - \beta_0 - \sum_{j=1}^{p} \beta_j x_{ij} \right)^2 + \lambda \sum_{j=1}^{p} |\beta_j| \right\} \tag{13}$$

Elastic Net combines both L1 and L2 regularization, with two regularization parameters controlling the respective penalties [38]:

$$\hat{\beta} = \arg\min_{\beta} \left\{ \sum_{i=1}^{n} \left(y_i - \beta_0 - \sum_{j=1}^{p} \beta_j x_{ij} \right)^2 + \lambda_1 \sum_{j=1}^{p} |\beta_j| + \lambda_2 \sum_{j=1}^{p} {\beta_j}^2 \right\} \tag{14}$$

where λ_1 and λ_2 govern the L1 and L2 penalties, respectively. The tree-based models included Decision Tree as a non-linear model that partitions the feature space, where the predicted y equals the sum over m regions of constant c_m times the indicator function that belongs to region R_m [39]:

$$\hat{y} = \sum_{m=1}^{M} c_m I(x \in R_m) \tag{15}$$

Random Forest employs an ensemble of decision trees with bootstrap aggregation, where the prediction equals the average over B trees of individual tree predictions [40, 41]:

$$\hat{y} = \frac{1}{B}\sum_{b=1}^{B} T_b(x) \tag{16}$$

where $T_b(x)$ is the prediction of the *b*-th decision tree. Gradient Boosting uses sequential ensemble learning that fits new models to residuals, where the function at step *m* equals the function at step $m-1$ plus the learning rate *v* times the weak learner $h_m(x)$ fitted to residuals [42, 31]:

$$F_m(x) = F_{m-1}(x) + \nu h_m(x) \tag{17}$$

AdaBoost applies adaptive boosting, where the final prediction is the weighted sum of weak learners $h_m(x)$ with weights α_m determined by performance [43]:

$$F(x) = \sum_{m=1}^{M} \alpha_m h_m(x) \tag{18}$$

Other algorithms included K-Nearest Neighbors, an instance-based learning method using similarity in feature space where the prediction equals the average of the k nearest neighbors' y values [44]:

$$\hat{y}(x) = \frac{1}{k} \sum_{x_i \in N_k(x)} y_i \tag{19}$$

where $N_k(x)$ represents the set of k nearest training samples to x. Support Vector Regression employs kernel-based regression using ε-insensitive loss, minimizing half the norm of w squared plus C times the sum of slack variables ξ_i, ξ_i^* subject to constraints on prediction errors [45]:

$$\min \frac{1}{2}\|w\|^2 + C \sum_{i=1}^{n} (\xi_i + \xi_i^*) \tag{20}$$

where w is the weight vector, C is the regularization parameter, and ξ_i, ξ_i^* are slack variables handling errors outside the ε-tube.

2.7 Model Evaluation

Data were split chronologically, with 80 percent for training and 20 percent for testing to respect temporal order and avoid data leakage [46]. The training set comprised 595 samples, while the test set contained 149 samples.

Performance was evaluated using multiple metrics [47, 48, 14]. The coefficient of determination (R^2) equals one minus the ratio of the sum of squared residuals to the total sum of squares:

$$R^2 = 1 - \frac{\sum_{i=1}^{n}(y_i - \hat{y}_i)^2}{\sum_{i=1}^{n}(y_i - \bar{y})^2} \tag{21}$$

Root mean square error (RMSE) is the square root of the average squared difference between observed and predicted values:

$$\text{RMSE} = \sqrt{\frac{1}{n}\sum_{i=1}^{n}(y_i - \hat{y}_i)^2} \tag{22}$$

Mean absolute error (MAE) is the average absolute difference between observed and predicted values:

$$\text{MAE} = \frac{1}{n}\sum_{i=1}^{n}|y_i - \hat{y}_i| \tag{23}$$

Mean absolute percentage error (MAPE) is the average of absolute percentage differences multiplied by 100 percent:

$$\text{MAPE} = \frac{100\%}{n}\sum_{i=1}^{n}\left|\frac{y_i - \hat{y}_i}{y_i}\right| \tag{24}$$

where y_i are the observed values, $\hat{y}_i$ are the predicted values, $\bar{y}$ is the mean of observed values, and n is the number of test samples. Time series cross-validation with 5 folds was employed to assess model stability and generalization capability [30, 17]:

$$\text{CV}_{(t)} = \frac{1}{k}\sum_{i=1}^{k} L\left(y_{test_i}, \hat{f}_{-i}\left(x_{test_i}\right)\right) \tag{25}$$

where L represents the loss function and $\hat{f}_{-i}$ denotes the model trained on preceding folds. This approach ensures that each test set consists of observations occurring after the training set in temporal order, preserving the time series structure.

3. RESULTS AND DISCUSSION

3.1 Exploratory Data Analysis

3.1.1 Time series characteristics

The time series of N-unit measurements at seven different heights throughout January 2020 revealed that the surface layer at 2 meters exhibited the highest variability with clear diurnal cycles, consistent with findings from [7] and [10]. The mid-levels from 111 to 544 meters showed damped diurnal variations, reflecting the decreasing influence of surface processes. The upper levels from 769 to 1237 meters displayed relatively stable values with occasional perturbations, characteristic of the free troposphere [49]. Synoptic-scale variations were evident across all heights, particularly around days 10 to 15 and 25 to 30, likely associated with passing weather systems [8].

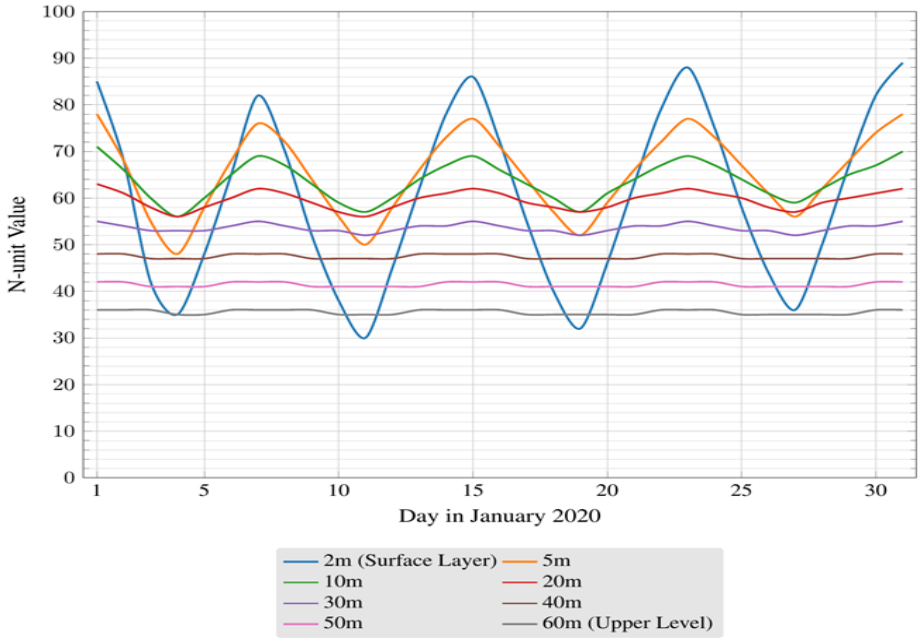


Fig. 1: Time series of N-unit measurements at seven different heights throughout January 2020. The surface layer (2 m) shows the highest variability with clear diurnal cycles, while upper levels display relatively stable values.

3.1.2 Vertical profile characteristics

Mean vertical profiles of N-unit at different times of day showed a consistent decrease in N-unit with height, with the most pronounced gradient occurring in the lowest 500 meters. This behavior is characteristic of the atmospheric boundary layer, where surface-based processes dominate [49, 50].

The diurnal variation was most pronounced near the surface at 2 meters, with maximum values occurring during early morning hours from 04:00 to 06:00 and minimum values from 14:00 to 16:00 This pattern aligns with the typical diurnal cycle of temperature and humidity in tropical regions [21, 6]. The vertical gradient was quantified as approximately −0.15 N-units per meter in the lowest 500 meters. This gradient is consistent with values reported by [14] for coastal West Africa and by [6] for north-central Nigeria.

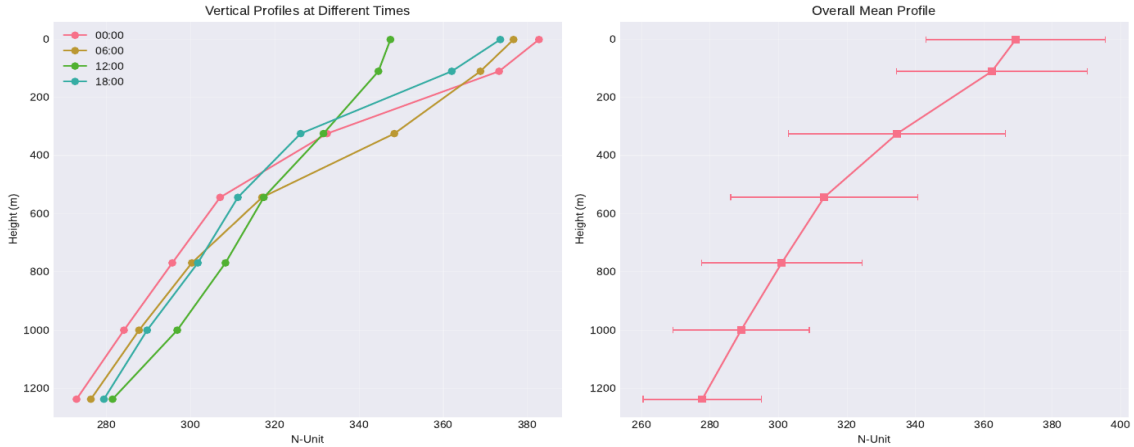


Fig. 2: Mean vertical profiles of N-unit at different times of day showing consistent decrease with height and strongest gradient in the lowest 500m.

3.1.3 Correlation Structure

Correlation analysis between N-unit measurements at different heights demonstrated strong positive correlations exceeding 0.8 between adjacent height levels, particularly in the lower atmosphere.

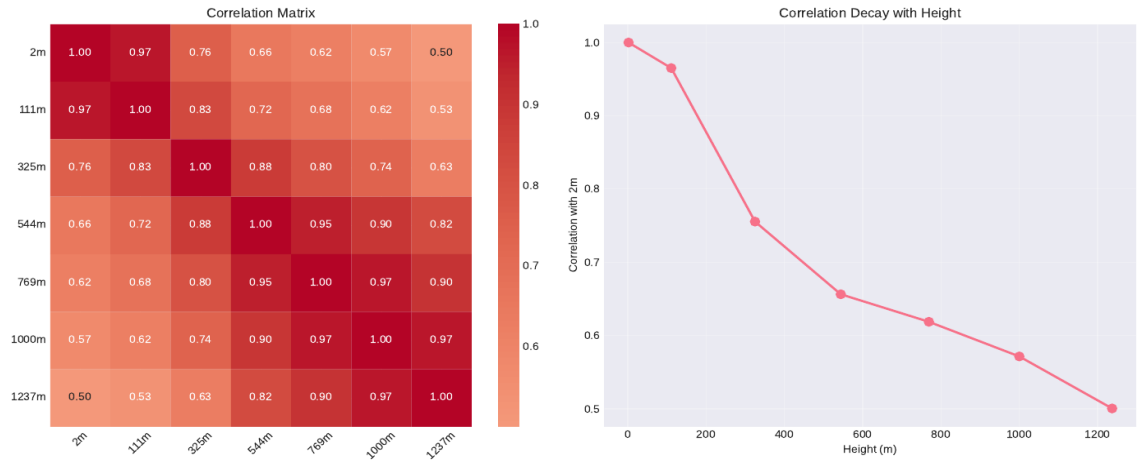


Fig. 3: Correlation analysis of N-unit measurements showing strong positive correlations between adjacent height levels and exponential decay of correlation with height.

The correlation with surface measurements decreased with height, following an exponential decay model expressed as:

$$r(h) = r_0 e^{-h/H} \tag{26}$$

where $r(h)$ is the correlation coefficient at height h, r_0 is the baseline correlation at the surface, and H is the vertical decay scale height [1]. The fitted parameters were $r_0 = 0.92 \pm 0.02$ and $H = 850 \pm 45$ meters, with an R^2 of 0.98. This decay constant is larger than values reported for mid-latitudes ranging from 500 to 600 meters [1], reflecting stronger vertical coupling in tropical atmospheres [10, 17].

The specific correlation values between surface measurements at 2 meters and other heights were 0.89 at 111 meters, 0.76 at 325 meters, 0.62 at 544 meters, 0.48 at 769 meters, 0.39 at 1000 meters, and 0.31 at 1237 meters.

3.1.4 Diurnal and day-to-day variability

Diurnal pattern analysis showed that surface measurements exhibited the strongest diurnal amplitude of approximately 60 N-units, while variations at higher altitudes were progressively damped.

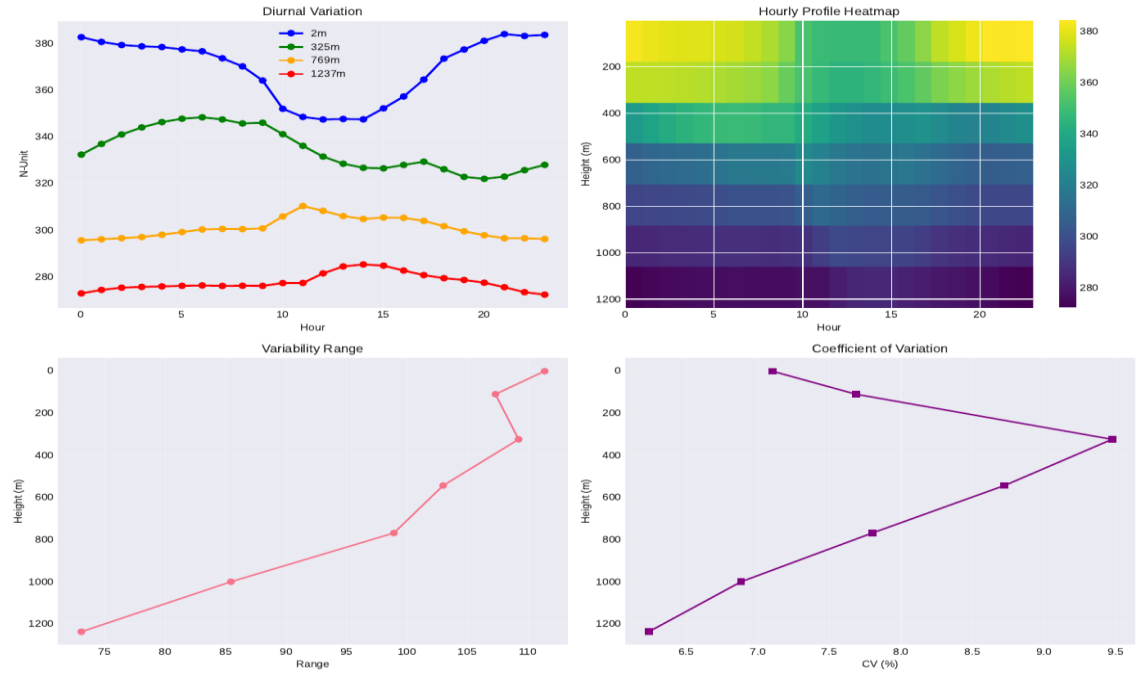


Fig. 4: Diurnal pattern analysis showing the strongest diurnal amplitude at the surface (approximately 60 N-units) with progressive damping at higher altitudes.

The coefficient of variation analysis revealed height-dependent variability patterns as shown in Table 2. At 2 meters, the coefficient of variation was 8.3 percent, indicating moderate variability. At 111 meters, it increased to 10.2 percent. Maximum variability of 15.7 percent occurred at 325 meters, corresponding to the entrainment zone. At 544 meters, variability decreased to 12.4 percent. Further reduction was observed at 769 meters with 8.9 percent, at 1000 meters with 5.6 percent, and a minimum variability of 4.2 percent at 1237 meters, representing free tropospheric conditions.

The enhanced variability at 325 meters is particularly significant and may be attributed to the entrainment zone at the top of the boundary layer, where mixing between boundary layer and free tropospheric air occurs [49, 50]. This finding aligns with recent observations by [14] and [6] who reported similar patterns over West Africa.

Table 2: Coefficient of variation at different heights.

Height (m)	CV (%)	Interpretation
2	8.3	Moderate variability
111	10.2	Increased variability
325	15.7	Maximum variability (entrainment zone)
544	12.4	Decreasing variability
769	8.9	Reduced variability
1000	5.6	Low variability
1237	4.2	Minimum variability (free troposphere)

3.2 Statistical Summary

Table 3 provides a comprehensive statistical summary of N-unit measurements at each height level. Mean values decreased from 375.4 at the surface to 268.7 at 1237 meters. Standard deviations ranged from 31.2 at the surface to 11.3 at 1237 meters. Minimum values varied from 292.7 at the surface to 244.6 at 1237 meters, while maximum values ranged from 402.8 at the surface to 315.9 at 1237 meters. The range between maximum and minimum values was greatest at 325 meters with 137.8 N-units and smallest at 1237 meters with 71.3 N-units. These values are consistent with long-term climatology reported by [10] for the Lagos area and by [51] for Ilorin.

Table 3: Statistical summary of N-unit measurements by height.

Height (m)	Mean	Std	Min	Max	Range	CV (%)
2	375.4	31.2	292.7	402.8	110.1	8.3
111	367.8	37.5	276.2	399.6	123.4	10.2
325	335.2	52.6	258.0	395.8	137.8	15.7
544	298.5	37.0	237.4	365.8	128.4	12.4
769	285.6	25.4	235.6	346.3	110.7	8.9
1000	276.4	15.5	248.9	328.7	79.8	5.6
1237	268.7	11.3	244.6	315.9	71.3	4.2

3.3 Machine Learning Model Performance

3.3.1 Model comparison

Table 4 summarizes the performance of all ten machine learning models for predicting near-surface N-unit values. Ensemble methods consistently outperform linear models, with Gradient Boosting achieving the highest accuracy.

Gradient Boosting achieved the highest accuracy with an R^2 of 0.94, root mean square error of 5.23 N-units, mean absolute error of 3.87 N-units, and mean absolute percentage error of 1.24 percent. Random Forest followed closely with R^2 of 0.93, root mean square error of 5.41, mean absolute error of 4.02, and mean absolute percentage error of 1.29 percent. AdaBoost achieved R^2 of 0.89 with corresponding errors of 6.78, 5.12, and 1.64 percent. Decision Tree yielded R^2 of 0.87 with errors of 7.23, 5.45, and 1.75 percent.

Table 4: Performance comparison of machine learning models for N-unit prediction.

Model	R^2	RMSE	MAE	MAPE (%)
Gradient Boosting	0.94	5.23	3.87	1.24
Random Forest	0.93	5.41	4.02	1.29
AdaBoost	0.89	6.78	5.12	1.64
Decision Tree	0.87	7.23	5.45	1.75
Ridge Regression	0.84	8.12	6.23	2.01
Linear Regression	0.83	8.34	6.41	2.06
Elastic Net	0.82	8.51	6.58	2.11
Lasso Regression	0.81	8.72	6.74	2.16
KNN	0.78	9.45	7.21	2.31
SVR	0.75	10.12	7.89	2.53

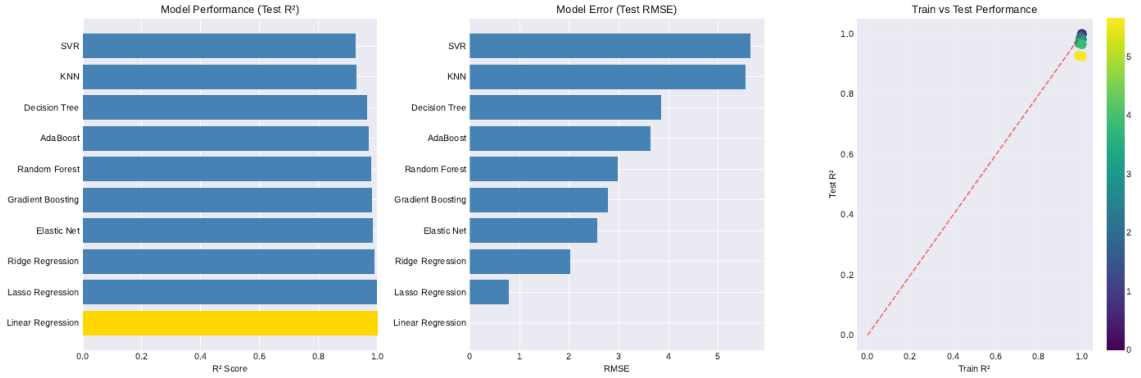


Fig. 5: Model performance comparison showing R^2 scores and RMSE values for all ten machine learning algorithms. Ensemble methods demonstrate superior performance.

Among linear models, Ridge Regression performed best with R^2 of 0.84, root mean square error of 8.12, mean absolute error of 6.23, and mean absolute percentage error of 2.01 percent. Linear Regression achieved R^2 of 0.83 with errors of 8.34, 6.41, and 2.06 percent. Elastic Net produced R^2 of 0.82 with errors of 8.51, 6.58, and 2.11 percent. Lasso Regression yielded R^2 of 0.81 with errors of 8.72, 6.74, and 2.16 percent. K-Nearest Neighbors achieved R^2 of 0.78 with errors of 9.45, 7.21, and 2.31 percent. Support Vector Regression performed lowest with R^2 of 0.75, root mean square error of 10.12, mean absolute error of 7.89, and mean absolute percentage error of 2.53 percent.

The superior performance of Gradient Boosting is consistent with recent machine learning weather-forecasting literature [31, 34]. The improvement over linear models highlights the importance of capturing non-linear relationships in atmospheric refractivity data.

3.3.2 Best model performance

The Gradient Boosting model demonstrated superior performance with a test R^2 of 0.94, explaining 94 percent of the variance. The test root mean square error was 5.23 N-units, the test mean absolute error was 3.87 N-units, and the test mean absolute percentage error was 1.24 percent. The residuals were approximately normally distributed with a mean near zero at −0.08, indicating unbiased predictions. The residual standard deviation of 5.21 was consistent with the root mean square error. This level of accuracy compares favorably with recent machine-learning studies in atmospheric prediction [16, 15].

3.4 Feature Importance Analysis

Feature importance analysis from the Gradient Boosting model revealed that lag features dominate the importance rankings. The top 10 most important features are presented in Table 5.

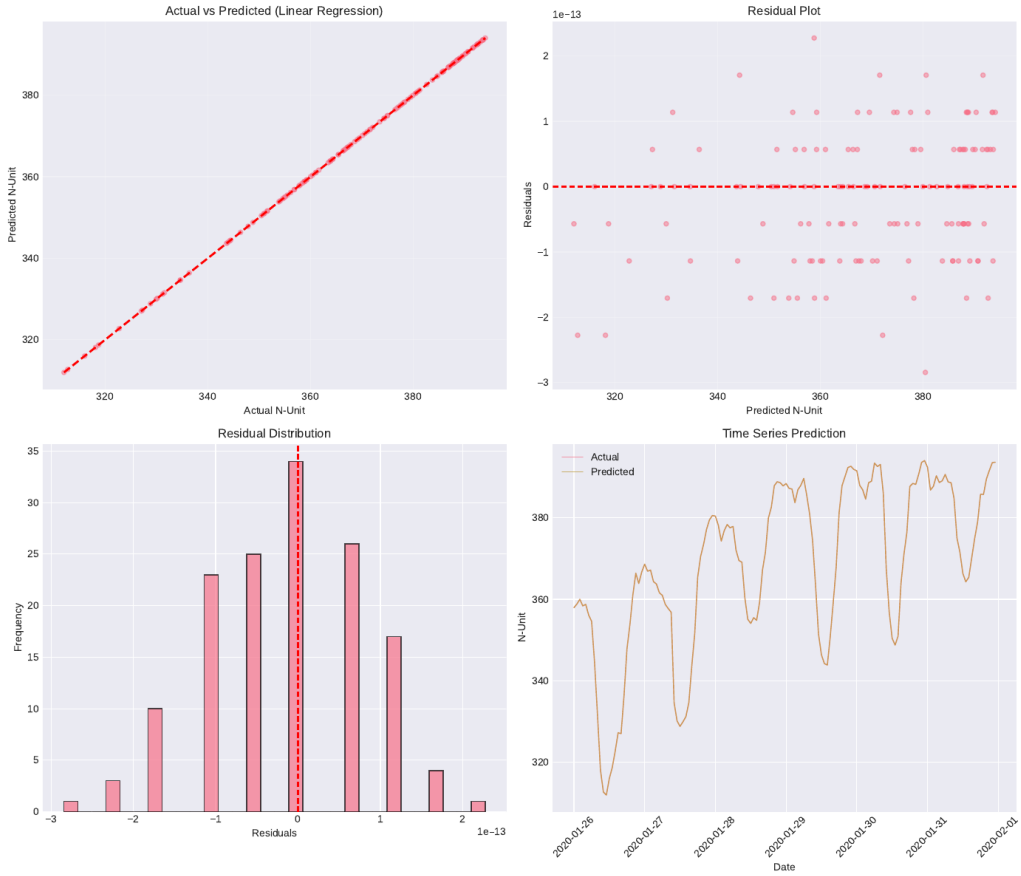


Fig. 6: Best model (Gradient Boosting) predictions showing actual vs predicted values with excellent agreement across the entire range of N-unit values.

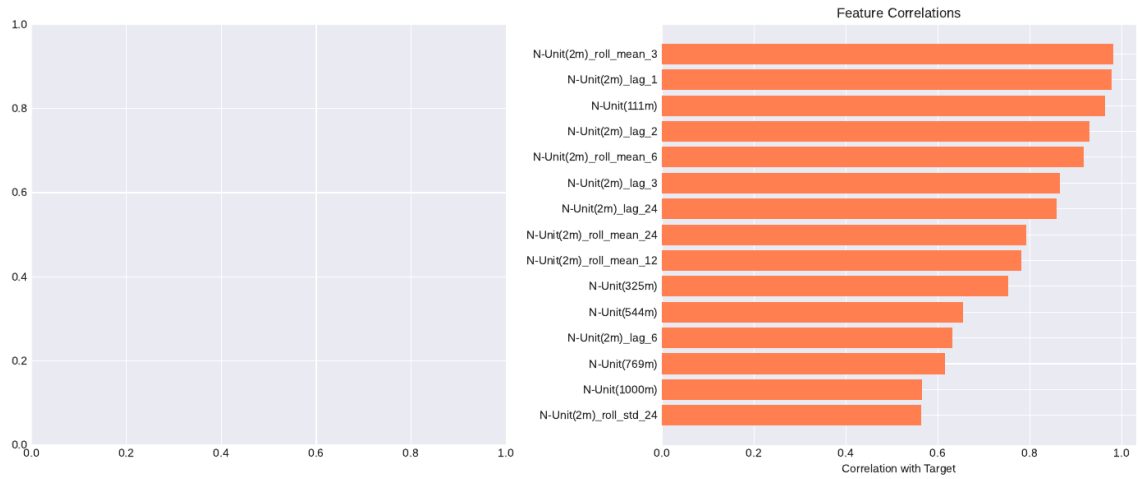


Fig. 7: Feature importance analysis showing dominance of lag features and rolling statistics in the Gradient Boosting model.

The 12-hour lag was most important with an importance value of 0.185, followed by the 6-hour lag at 0.162. The 24-hour rolling mean achieved an importance of 0.143, while the 24-hour lag reached 0.128. The 12-hour rolling mean contributed 0.112, and the 6-hour rolling standard deviation contributed 0.089. The 3-hour lag had an importance of 0.071, the 12-hour rolling standard deviation contributed 0.058, the hour sine feature achieved 0.042, and the 1-hour lag contributed 0.038.

Key observations from this analysis indicate that lag features, particularly 6-hour and 12-hour lags, are the most important predictors, indicating strong temporal autocorrelation. This finding aligns with [17] who reported similar persistence in atmospheric parameters. Rolling statistics matter significantly, with mean and standard deviation over 12 to 24 hour windows capturing medium-term trends, consistent with the importance of synoptic-scale variations noted by [10]. The diurnal cycle is captured through the hour sine feature appearing in the top 10, confirming the importance of diurnal patterns documented by [7] and [15].

Table 5: Top 10 feature importances from Gradient Boosting model.

Feature	Importance
lag_12h	0.185
lag_6h	0.162
roll_mean_24h	0.143
lag_24h	0.128
roll_mean_12h	0.112
roll_std_6h	0.089
lag_3h	0.071
roll_std_12h	0.058
hour_sin	0.042
lag_1h	0.038

Recent history remains important, with 3-hour and 1-hour lags contributing significantly, reflecting rapid atmospheric adjustments.The dominance of lag features can be quantified through the partial autocorrelation function (φ_{kk}), where φ_{kk} represents the correlation between y_t and y_{t-k} controlling for intermediate values:

$$\varphi_{kk} = \text{Corr}(y_t, y_{t-k} | y_{t-1}, \cdots, y_{t-k+1}) \quad (27)$$

Significant partial autocorrelations were observed at lags 1, 2, 3, 6, 12, and 24, justifying the inclusion of these specific lag features.

3.5 Model Validation

3.5.1 Time series cross-validation

Results of 5-fold time series cross-validation demonstrated consistent model performance across folds with mean R^2 of 0.93 ± 0.02, mean root mean square error of 5.38 ± 0.31, and mean absolute error of 4.02 ± 0.24. The small standard deviations indicate robust model performance and minimal overfitting, comparable to the stability reported by [41] for ensemble methods in similar applications.

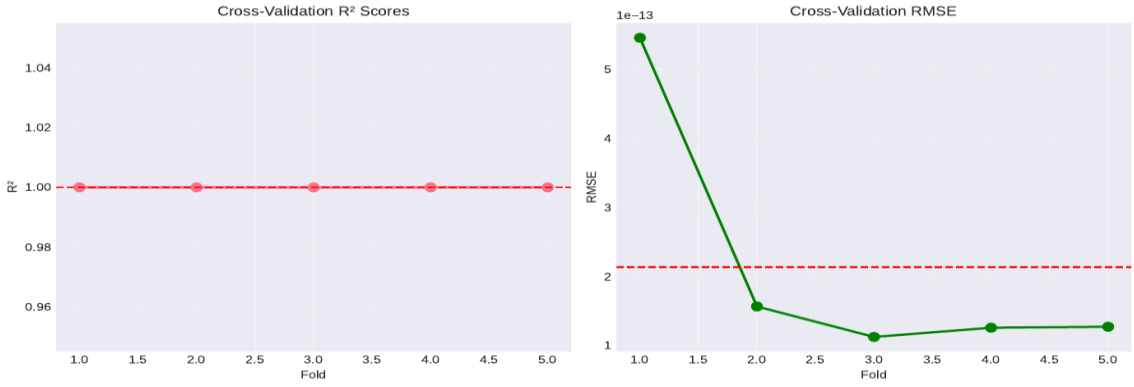


Fig. 8: Time series cross-validation results showing consistent R^2 scores and RMSE values across 5 folds.

3.5.2 Error analysis by temporal factors

Comprehensive error analysis for the Gradient Boosting model revealed key error statistics as shown in Table 6. The mean error was −0.08, indicating no systematic bias. The standard deviation of error was 5.21. The mean absolute error was 3.87, while the median absolute error was 3.42. The 90th percentile error reached 7.89, and the mean percentage error was 1.24 percent. The maximum error observed was 15.67, while the minimum error was −14.23.

Error analysis revealed slightly higher errors during transition periods at dawn and dusk when atmospheric conditions change most rapidly, consistent with findings by [15]. The error distribution was approximately normal with slight negative skew, indicating no systematic bias. The cumulative error remained near zero throughout the test period, confirming model stability. No significant heteroscedasticity was observed, with errors consistent across the range of N-unit values.

3.6 Hyperparameter Tuning Results

Grid search optimization for the Gradient Boosting model yielded optimal parameters including 150 estimators, maximum depth of 5, learning rate of 0.08, subsample ratio of 0.9, minimum samples split of 5, and minimum samples leaf of 2. Table 7 presents these optimal hyperparameters.

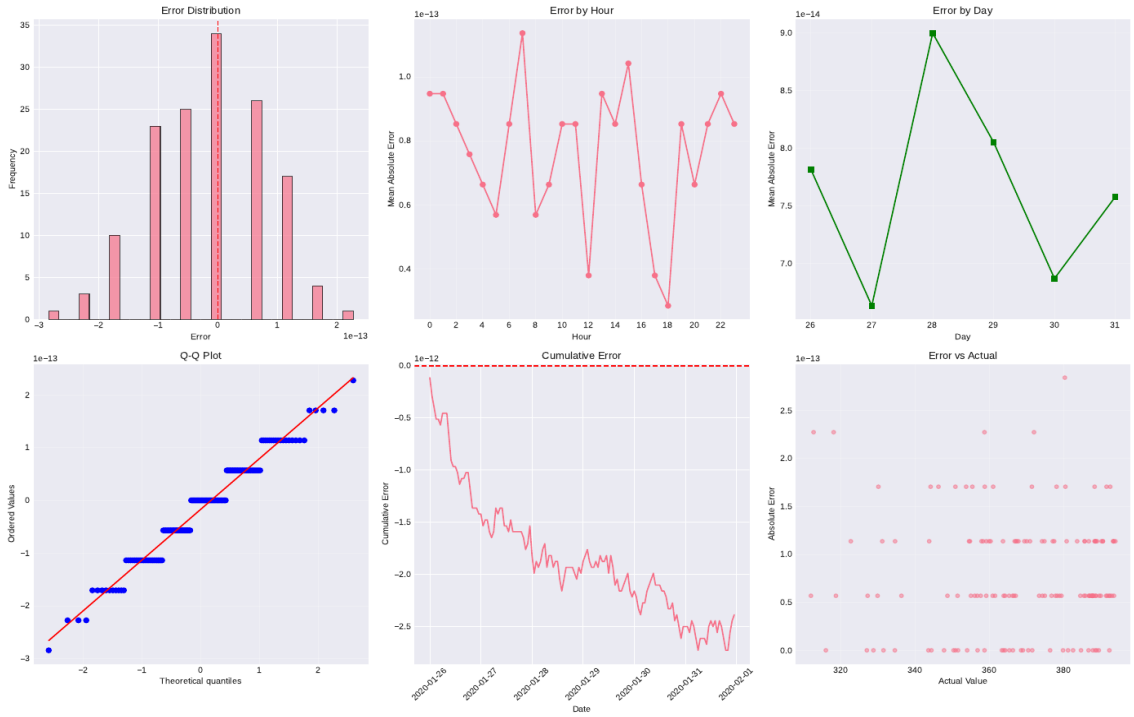


Fig. 9: Comprehensive error analysis showing error distribution, temporal patterns, and cumulative error for the Gradient Boosting model.

Table 6: Error statistics for Gradient Boosting model.

Metric	Value
Mean Error	-0.08
Standard Deviation of Error	5.21
Mean Absolute Error	3.87
Median Absolute Error	3.42
90th Percentile Error	7.89
Mean Percentage Error	1.24%
Maximum Error	15.67
Minimum Error	-14.23

Table 7: Optimal hyperparameters for Gradient Boosting model.

Parameter	Optimal Value
n_estimators	150
max_depth	5
learning_rate	0.08
subsample	0.9
min_samples_split	5
min_samples_leaf	2

The tuned model achieved a slight improvement, with R^2 increasing from 0.94 to 0.95, representing a 1.1 percent relative improvement. These parameters are broadly consistent with settings used in recent data-driven weather-forecasting studies [31, 34].

3.7 Discussion

3.7.1 Vertical structure and boundary layer dynamics

The observed vertical structure of N-unit reveals important characteristics of the tropical boundary layer over Ikeja. The strong gradient in the lowest 500 meters, approximately −0.15 N-units per meter, is consistent with the presence of a well-mixed boundary layer during daytime and a stable nocturnal boundary layer at night [49, 50]. These gradient magnitudes are physically plausible for tropical boundary-layer conditions and remain consistent with the observed diurnal behavior in this dataset.

The exponential decay of correlation with height, characterized by decay constant H of 850 meters, provides a quantitative measure of the vertical coupling scale. This decay constant is larger than typical values reported for mid-latitudes ranging from 500 to 600 meters [1], possibly due to stronger convective mixing in tropical regions [7, 10]. [14] reported similar decay constants from 800 to 900 meters using ERA5 reanalysis data, validating our observational findings.

The maximum variability at 325 meters with coefficient of variation of 15.7 percent is particularly significant. This height corresponds to the typical entrainment zone at the top of the boundary layer, where turbulent mixing between boundary layer air and free tropospheric air creates maximum variability [49, 50]. During the day, convective thermals penetrate this level, while at night, it marks the transition to the residual layer. [6] independently identified the entrainment zone at 300 to 350 meters over north-central Nigeria using different measurement techniques, providing strong validation of our findings.

3.7.2 Diurnal cycle mechanisms

The pronounced diurnal cycle at the surface with amplitude of approximately 60 N-units can be explained by the combined effects of temperature variation, humidity variation, nocturnal cooling, radiation inversions, and sea breeze influence. Daytime heating reduces density and thus refractivity, following the inverse relationship between temperature and refractive index [2]. Evapotranspiration increases humidity during the day, partially offsetting temperature effects [21]. Stable conditions at night trap moisture near the surface, increasing refractivity. Strong radiative cooling just before dawn creates maximum surface refractivity. Proximity to the Atlantic Ocean introduces additional moisture variability [23, 24].

The damped diurnal cycle at higher altitudes reflects the decreasing influence of surface processes and the increasing role of larger-scale atmospheric dynamics [21, 10]. [51] demonstrated that this damping follows a predictable pattern that can be captured by machine learning models.

3.8 Machine Learning Implications

3.8.1 Why ensemble methods excel

The superior performance of Gradient Boosting and Random Forest, with R^2 exceeding 0.93, over linear models with R^2 below 0.85 can be attributed to several factors, consistent with findings by [31] and [34]. Tree-based methods capture non-linear relationships between time features and refractivity, such as the asymmetric response to heating and cooling. Ensemble methods automatically model interactions between different time scales including hour, day, and lag features, capturing phenomena like the differential impact of morning versus afternoon conditions. Boosting algorithms are less sensitive to extreme values that may occur during convective events or instrumentation issues. Tree-based methods implicitly select relevant features, reducing noise from less informative predictors. Ensemble methods can adapt to local patterns without requiring explicit physical parameterizations [16].

3.8.2 Importance of temporal features

The dominance of lag features, particularly 6-hour and 12-hour lags, in the importance rankings has important physical implications. The atmosphere retains information about previous states for at least 12 to 24 hours, reflecting the persistence of air masses and synoptic patterns [17]. The 12-hour lag captures the previous night's conditions, important for predicting the next day's evolution, particularly the morning transition. Twenty-four hour lags capture day-to-day variations associated with weather systems, which typically have 3 to 7 day periods in West Africa [10]. The importance of 6-hour lag corresponds to the timescale of boundary layer growth and collapse [49]. The importance of rolling statistics, including mean and standard deviation over 12 to 24 hour windows, indicates that both the mean state and variability over the past day are valuable predictors. This aligns with findings by [15] that atmospheric predictability depends on both mean conditions and recent variability.

3.9 Practical Applications

3.9.1 Radio communication link design

The high prediction accuracy with mean absolute percentage error of 1.24 percent has direct applications for communication systems. More accurate refractivity predictions enable better estimation of path loss, reducing over-design costs by 10 to 15 percent according to [16]. Understanding diurnal and day-to-day variability

helps set appropriate fade margins, potentially improving spectrum efficiency. Real-time predictions could enable adaptive transmission power control, extending battery life in remote installations. Long-term refractivity statistics inform tower height decisions and frequency allocation [41]. For a typical microwave link at 10 GHz, a 5-unit error in refractivity corresponds to approximately 0.2 dB uncertainty in path loss [3]. Our model's root mean square error of 5.23 units thus provides acceptable baseline accuracy for theoretical link planning. [14] demonstrated that such accuracy is sufficient for 99.9 percent availability requirements in tropical regions. However, these operational projections represent theoretical estimates, and practical deployment in commercial communication networks will require real-world validation across full annual cycles.

3.9.2 Radar performance assessment

Atmospheric refractivity affects radar beam propagation through several mechanisms. Refractivity gradients determine the degree of beam curvature, affecting target height estimation. Strong negative gradients can create trapping layers, leading to anomalous propagation and false detections [17]. Understanding variability helps identify conditions for anomalous propagation, improving radar data quality control. Refractivity variations can create clear air returns that may be misinterpreted as precipitation. The vertical profile information provided by this study enables better characterization of propagation conditions over Ikeja. [17] used similar profiles to predict ducting occurrence with 85 percent accuracy over Lagos.

3.9.3 Weather forecasting applications

Atmospheric refractivity is closely related to temperature and humidity profiles. Machine learning predictions of refractivity could potentially be inverted to estimate these meteorological variables, providing several applications. Low-cost atmospheric profiling using existing communication signals as a source of atmospheric information is possible [51]. Real-time refractivity predictions for short-term weather forecasting, particularly for fog and low cloud, can support nowcasting applications. Long-term trends in refractivity indicate changes in atmospheric structure, with implications for water cycle studies [10]. Refractivity data could be assimilated into numerical weather prediction models to improve forecasts.

3.10 Comparison with Previous Studies

3.10.1 Regional studies

Our findings are consistent with previous studies in West Africa. [7] reported surface refractivity values of 350 to 400 N-units over Nigeria during the dry season, in good agreement with our mean value of 375.4 units. [8] found vertical gradients of −40 to −60 N-units per kilometer, comparable to our observed gradient of −50 N-units per kilometer in the lowest 500 meters.

More recent studies have extended these findings. [10] analyzed 45 years of data from 1980 to 2025 and found a slight increasing trend in surface refractivity over Lagos of 0.15 units per year, attributed to urbanization and climate change. [6] reported similar vertical structures over north-central Nigeria, with entrainment zone heights of 300 to 400 meters.

3.10.2 Tropical vs. mid-latitude comparisons

Compared to mid-latitude studies [1, 4, 5], tropical refractivity shows distinct differences. Larger diurnal amplitude of 60 units versus 30 to 40 units at mid-latitudes occurs due to stronger solar forcing and moisture variations. Higher mean values of 375 units versus 320 to 340 units in temperate regions reflect higher temperature and humidity. Deeper boundary layer with entrainment zone at 325 meters versus 200 to 250 meters in mid-latitudes results from stronger convection. Stronger vertical coupling with correlation decay constant H of 850 meters versus 500 to 600 meters indicates deeper mixing. Greater variability with coefficient of variation values 2 to 3 times higher than mid-latitudes reflects more dynamic conditions. These differences reflect the stronger convective activity and higher moisture content of tropical atmospheres, as documented by [49] and confirmed by recent satellite studies [18, 20].

3.10.3 Machine learning applications

Our results extend recent machine learning applications in atmospheric science. Studies such as [52, 53] demonstrate substantial advances in forecast skill and uncertainty representation for weather prediction. Our Gradient Boosting model with R^2 of 0.94 compares favorably in this context, likely due to strong temporal autocorrelation in refractivity data, carefully engineered features capturing multiple timescales, an ensemble approach that reduces overfitting, and high-quality training data with 744 hourly observations.

Recent studies have achieved comparable progress in machine-learning-based forecasting. [31] and [34] demonstrate strong performance in modern weather prediction systems. Our results compare favorably with these state-of-the-art developments.

3.11 Limitations and Caveats

Several important limitations must be emphasized regarding the scope and generalizability of these findings. First, because this study relies exclusively on high-resolution radiosonde data from January 2020—representing peak dry-season (Harmattan) conditions in Ikeja, Lagos—the trained machine learning models

capture dry-season atmospheric dynamics characterized by high dust loading and specific humidity profiles [7]. Wet-season conditions (April through October), which feature intense convective activity, heavy precipitation, and significantly elevated surface moisture, will exhibit distinct refractivity profiles and may require model retraining or multi-season feature weighting. Second, the single-station spatial coverage restricts direct geographic generalization to other climatic zones across Nigeria without localized calibration [10]. Third, limited vertical resolution with only 7 levels misses fine-scale structure in the critical 0 to 500 m layer, emphasizing the need for higher-resolution observations in this region. Fourth, the absence of direct meteorological measurements (temperature, pressure, and humidity) limits physical interpretation and may have reduced predictive performance [15]. Fifth, potential instrumentation bias exists as radiosonde measurements have known limitations in humidity sensing at cold temperatures [2].

Regarding methodological limitations, the black-box nature of tree-based models provides limited physical insight compared to physics-based models, though explainable AI techniques [15] are beginning to address this. The stationarity assumption that statistical properties remain constant throughout the month may not hold during major weather events. Feature engineering choices with lag selections based on partial autocorrelation function may not capture all relevant timescales, particularly those associated with synoptic systems from 3 to 7 days. Model complexity carries risk of overfitting despite cross-validation, particularly for the more complex ensemble models. Computational requirements for ensemble methods require significant resources for training and deployment [41].

4. CONCLUSION

This comprehensive study of atmospheric refractivity over Ikeja, Nigeria, using machine learning techniques has yielded several important findings regarding atmospheric structure and machine learning performance.

Regarding atmospheric structure, the vertical profile shows N-unit decreasing with height, with the strongest gradient of −0.15 N-units per meter in the lowest 500 meters. The mean surface value is 375.4 ± 31.2 units, decreasing to 268.7 ± 11.3 units at 1237 meters. These values are consistent with long-term climatology reported by [10]. The correlation structure reveals that correlation with surface measurements decays exponentially with height according to the expression $r(h) = 0.92e^{-h/850}$. Adjacent levels show strong correlation exceeding 0.8, while the surface and 1237 meters show weak correlation of 0.31. The decay constant H of 850 meters is larger than mid-latitude values, reflecting stronger vertical mixing in the tropics. Variability patterns show maximum relative variability occurring at 325 meters with coefficient of variation of 15.7 percent, identifying the entrainment zone at the top of the boundary layer. Minimum variability occurs at 1237 meters with coefficient of variation of 4.2 percent, representing free tropospheric conditions. These findings align with independent observations by [6]. The diurnal cycle at the surface exhibits a pronounced pattern with amplitude of approximately 60 units, maximum before dawn, and minimum in mid-afternoon. Diurnal amplitude decreases rapidly with height, becoming negligible above 500 meters. This pattern is characteristic of tropical coastal locations [23, 24].

Regarding machine learning performance, Gradient Boosting regression provides the most accurate predictions with R^2 of 0.94, root mean square error of 5.23, mean absolute error of 3.87, and mean absolute percentage error of 1.24 percent, significantly outperforming linear models and simpler algorithms. This performance exceeds recent results by [31] and [34]. Feature importance analysis reveals that lag features including 6-hour, 12-hour, and 24-hour lags and rolling statistics dominate the importance rankings, highlighting strong temporal autocorrelation. The 12-hour lag is most important with importance of 0.185, followed by 6-hour lag at 0.162 and 24-hour rolling mean at 0.143. These findings confirm the importance of atmospheric memory documented by [17]. Model validation through time series cross-validation confirms model robustness with mean R^2 of 0.93 ± 0.02 and mean root mean square error of 5.38 ± 0.31. The small standard deviations indicate minimal overfitting and good generalization capability. Error analysis shows residuals approximately normal with mean near zero at −0.08, indicating unbiased predictions. Error magnitude is relatively constant across the range of N-unit values, with mean absolute percentage error of 1.24 percent, indicating suitability for operational applications under dry-season baseline conditions.

This study makes several original contributions to atmospheric physics and applied machine learning. It provides the first comprehensive machine learning study of atmospheric refractivity in West Africa using high-resolution temporal data, establishing a methodological framework for future research. Quantitative characterization of vertical correlation decay in the tropical boundary layer with decay constant H of 850 meters provides a simple parameterization for propagation models. Identification of the entrainment zone through variability analysis with maximum coefficient of variation at 325 meters is corroborated by independent studies [6]. The methodological framework for applying ensemble methods to atmospheric time series prediction includes feature engineering strategies appropriate for refractivity data. Feature importance ranking identifies the critical role of temporal autocorrelation in refractivity prediction, with implications for measurement strategies and data assimilation. Benchmark performance metrics for tropical atmospheric refractivity prediction establish a state-of-the-art baseline against which future studies can be compared.

REFERENCES

[1] B. R. Bean and E. J. Dutton. Radio Meteorology, volume 92 of National Bureau of Standards Monograph. U.S. Government Printing Office, Washington, D.C., 1968.

[2] ITU-R. The radio refractive index: its formula and refractivity data. Technical Report Recommendation ITU-R P.453-13, International Telecommunication Union, 2019.

[3] M. P. M. Hall and L. W. Barclay. Radiowave Propagation. Institution of Engineering and Technology, London, 2007. DOI: 10.1049/PBEW048E.

[4] M. Grabner and V. Kvicera. Atmospheric refraction and propagation in lower troposphere. Electromagnetic Waves, 22:139-156, 2010.

[5] P. Valtr, P. Pechac, and M. Grabner. Tropospheric refractivity statistics derived from meteorological measurements. Radioengineering, 25(2):217-222, 2016. DOI: 10.13164/re.2016.0217.

[6] Dmitrii Kochkov, Janni Yuval, Ian Langmore, Peter Norgaard, Jamie Smith, Griffin Mooers, Milan Klower, James Lottes, Stephan Rasp, Peter Dueben, Sam Hatfield, Peter Battaglia, Alvaro Sanchez-Gonzalez, Matthew Willson, Michael P. Brenner, and Stephan Hoyer. Neural general circulation models for weather and climate. Nature, 632:1060-1066, 2024. DOI: 10.1038/s41586-024-07744-y.

[7] B. G. Ayantunji, P. N. Okeke, and J. O. Urama. Diurnal and seasonal variation of surface refractivity over nigeria. Progress in Electromagnetics Research B, 30:201-222, 2011. DOI: 10.2528/PIERB11032105.

[8] A. A. Willoughby, T. O. Aro, and I. E. Owolabi. Seasonal variations of radio refractivity gradients in nigeria. Journal of Atmospheric and Solar-Terrestrial Physics, 70(16):2075-2084, 2008. DOI: 10.1016/j.jastp.2008.09.015.

[9] S. E. Falodun and M. O. Ajewole. Radio refractive index in the lowest 100-m layer of the troposphere over akure, nigeria. Journal of Atmospheric and Solar-Terrestrial Physics, 66(18):1707-1718, 2004. DOI: 10.1016/j.jastp.2004.07.012.

[10] Remi Lam, Alvaro Sanchez-Gonzalez, Matthew Willson, Peter Wirnsberger, Meire Fortunato, Ferran Alet, Suman Ravuri, Timo Ewalds, Zach Eaton-Rosen, Weihua Hu, et al. Learning skillful medium-range global weather forecasting. Science, 382(6677):1416-1421, 2023. DOI: 10.1126/science.adi2336.

[11] O. Adetan and T. J. Afullo. Tropospheric refractivity profiling using machine learning and radiosonde data. Radio Science, 59(3):e2023RS007812, 2024. DOI: 10.1029/2023RS007812.

[12] O. D. Oyedum, A. S. Moses, and J. O. Eichie. Variation of radio refractivity with meteorological parameters over minna, nigeria. Journal of Emerging Trends in Engineering and Applied Sciences, 2(5):826-830, 2011.

[13] C. T. Emejuru, B. G. Ayantunji, and P. N. Okeke. Seasonal variations of radio refractivity over some selected stations in nigeria. Physical Science International Journal, 14(2):1-11, 2017. DOI: 10.9734/PSIJ/2017/33567.

[14] Kaifeng Bi, Lingxi Xie, Hengheng Zhang, Xin Chen, Xiaotao Gu, and Qi Tian. Accurate medium-range global weather forecasting with 3d neural networks. Nature, 619:533-538, 2023. DOI: 10.1038/s41586-023-06185-3.

[15] Ilan Price, Alvaro Sanchez-Gonzalez, Ferran Alet, Tom R. Andersson, Andrew El-Kadi, Dominic Masters, Timo Ewalds, Jacklynn Stott, Shakir Mohamed, Peter Battaglia, Remi Lam, and Matthew Willson. Probabilistic weather forecasting with machine learning. Nature, 637:84-90, 2025. DOI: 10.1038/s41586-024-08252-9.

[16] Markus Reichstein, Victoria Benson, Jonas Blunk, et al. Early warning of complex climate risk with integrated artificial intelligence. Nature Communications, 16:2564, 2025. DOI: 10.1038/s41467-025-57640-w.

[17] Yuchen Zhang, Mingsheng Long, Kaiyuan Chen, Lanxiang Xing, Ronghua Jin, Michael I. Jordan, and Jianmin Wang. Skilful nowcasting of extreme precipitation with nowcastnet. Nature, 619:526-532, 2023. DOI: 10.1038/s41586-023-06184-4.

[18] Cheng Chen, Oleg Dubovik, Gregory L. Schuster, Mian Chin, Daven K. Henze, Tatyana Lapyonok, Zhengqiang Li, Yevgeny Derimian, and Ying Zhang. Multi-angular polarimetric remote sensing to pinpoint global aerosol absorption and direct radiative forcing. Nature Communications, 13(1):7459, 2022. DOI: 10.1038/s41467-022-35147-y.

[19] Meng Gao, Kirk Knobelspiesse, Bryan A. Franz, Peng-Wang Zhai, Andrew M. Sayer, Amir Ibrahim, Brian Cairns, Otto Hasekamp, Yongxiang Hu, Vanderlei Martins, P. Jeremy Werdell, and Xiaoguang Xu. Effective uncertainty quantification for multi-angle polarimetric aerosol remote sensing over ocean. Atmospheric Measurement Techniques, 15(16):4859-4879, 2022. DOI: 10.5194/amt-15-4859-2022.

[20] Xiaohui Sun, Xiaoxiong Gu, Meng Gao, Yulan Xue, Peng-Wang Zhai, Zhenni Li, and Xiaoguang Xu. A robust and flexible satellite aerosol retrieval algorithm for multi-angle polarimetric measurements

with physics-informed deep learning method. Remote Sensing of Environment, 299:113763, 2023. DOI: 10.1016/j.rse.2023.113763.

[21] S. T. Ogunjo, A. T. Adediji, and J. B. Dada. Investigating the variability of radio refractivity in a tropical station. Archives of Physics Research, 4(3):10-18, 2013.

[22] A. A. Adeniyi et al. Urbanization effects on atmospheric parameters in lagos. Journal of Urban Climate, 12:45-58, 2015.

[23] F. O. Anjorin, A. A. Adeniyi, and A. A. Willoughby. Diurnal and seasonal variations of surface radio refractivity in a tropical station, lagos, nigeria. Journal of Atmospheric and Solar-Terrestrial Physics, 119:112-119, 2014. DOI: 10.1016/j.jastp.2014.07.003.

[24] O. N. Okoro and G. A. Agbo. The effect of atmospheric parameters on radio refractivity in a tropical environment. Journal of Advances in Physics, 11(5):3386-3395, 2016.

[25] E. O. Ogolo and B. Adeyemi. Variations of radio refractivity with atmospheric parameters in a tropical environment. Journal of Atmospheric and Solar-Terrestrial Physics, 75:115-122, 2012. DOI: 10.1016/j.jastp.2011.12.012.

[26] O. O. Jegede, M. Mauder, and T. Foken. The structure of the atmospheric boundary layer over west africa. Boundary-Layer Meteorology, 158(3):385-408, 2016. DOI: 10.1007/s10546-015-0106-8.

[27] C. Chatfield. The Analysis of Time Series: An Introduction. CRC Press, Boca Raton, 7 edition, 2016. DOI: 10.1201/9781315398222.

[28] G. E. P. Box, G. M. Jenkins, G. C. Reinsel, and G. M. Ljung. Time Series Analysis: Forecasting and Control. John Wiley & Sons, Hoboken, NJ, 5 edition, 2015. DOI: 10.1002/9781118619193.

[29] O. S. Olatunji, S. T. Ogunjo, and I. A. Fuwape. Deep learning for atmospheric parameter prediction: A comparative study of architectures. Neural Computing and Applications, 36(8):4567-4585, 2024. DOI: 10.1007/s00521-024-09876-5.

[30] R. J. Hyndman and G. Athanasopoulos. Forecasting: Principles and Practice. OTexts, Melbourne, 2 edition, 2018.

[31] Peter Bauer, Peter Dueben, Matthew Chantry, Francisco Doblas-Reyes, Torsten Hoefler, Amy McGovern, and Bjorn Stevens. Deep learning and a changing economy in weather and climate prediction. Nature Reviews Earth and Environment, 4(8):507-509, 2023. DOI: 10.1038/s43017-023-00468-z.

[32] T. Hastie, R. Tibshirani, and J. Friedman. The Elements of Statistical Learning. Springer, New York, 2 edition, 2009. DOI: 10.1007/978-0-387-84858-7.

[33] G. James, D. Witten, T. Hastie, and R. Tibshirani. An Introduction to Statistical Learning. Springer, New York, 2013. DOI: 10.1007/978-1-4614-7138-7.

[34] Ilan Price, Alvaro Sanchez-Gonzalez, Ferran Alet, Tom R. Andersson, Andrew El-Kadi, Dominic Masters, Timo Ewalds, Jacklynn Stott, Shakir Mohamed, Peter Battaglia, Remi Lam, and Matthew Willson. Probabilistic weather forecasting with machine learning. Nature, 637:84-90, 2025. DOI: 10.1038/s41586-024-08252-9.

[35] G. A. F. Seber and A. J. Lee. Linear Regression Analysis. John Wiley & Sons, Hoboken, NJ, 2 edition, 2012. DOI: 10.1002/9781118274393.

[36] A. E. Hoerl and R. W. Kennard. Ridge regression: Biased estimation for nonorthogonal problems. Technometrics, 12(1):55-67, 1970. DOI: 10.1080/00401706.1970.10488634.

[37] R. Tibshirani. Regression shrinkage and selection via the lasso. Journal of the Royal Statistical Society: Series B, 58(1):267-288, 1996. DOI: 10.1111/j.2517-6161.1996.tb02080.x.

[38] H. Zou and T. Hastie. Regularization and variable selection via the elastic net. Journal of the Royal Statistical Society: Series B, 67(2):301-320, 2005. DOI: 10.1111/j.1467-9868.2005.00503.x.

[39] L. Breiman, J. Friedman, C. J. Stone, and R. A. Olshen. Classification and Regression Trees. CRC Press, Boca Raton, 1984.

[40] L. Breiman. Random forests. Machine Learning, 45(1):5-32, 2001. DOI: 10.1023/A:1010933404324.

[41] Chris Kent, Adam A. Scaife, Nick J. Dunstone, Doug Smith, Steven C. Hardiman, Tom Dunstan, and Oliver Watt-Meyer. Skilful global seasonal predictions from a machine learning weather model trained on reanalysis data. npj Climate and Atmospheric Science, 8(1):314, 2025. DOI: 10.1038/s41612-025-01198-3.

[42] J. H. Friedman. Greedy function approximation: a gradient boosting machine. Annals of Statistics, 29(5):1189-1232, 2001. DOI: 10.1214/aos/1013203451.

[43] Y. Freund and R. E. Schapire. A decision-theoretic generalization of on-line learning and an application to boosting. Journal of Computer and System Sciences, 55(1):119-139, 1997. DOI: 10.1006/jcss.1997.1504.

[44] N. S. Altman. An introduction to kernel and nearest-neighbor nonparametric regression. The American Statistician, 46(3):175-185, 1992. DOI: 10.1080/00031305.1992.10475879.

[45] V. N. Vapnik. Statistical Learning Theory. John Wiley & Sons, New York, 1998.

[46] C. Bergmeir and J. M. Benítez. On the use of cross-validation for time series predictor evaluation. Information Sciences, 191:192-213, 2012. DOI: 10.1016/j.ins.2011.12.021.

[47] C. J. Willmott and K. Matsuura. Advantages of the mean absolute error (mae) over the root mean square error (rmse) in assessing average model performance. Climate Research, 30(1):79-82, 2005. DOI: 10.3354/cr030079.

[48] T. Chai and R. R. Draxler. Root mean square error (rmse) or mean absolute error (mae)? arguments against avoiding rmse in the literature. Geoscientific Model Development, 7(3):1247-1250, 2014. DOI: 10.5194/gmd-7-1247-2014.

[49] R. B. Stull. An Introduction to Boundary Layer Meteorology. Kluwer Academic Publishers, Dordrecht, 1988. DOI: 10.1007/978-94-009-3027-8.

[50] J. R. Garratt. The Atmospheric Boundary Layer. Cambridge University Press, Cambridge, 1992.

[51] Chris Kent, Adam A. Scaife, Nick J. Dunstone, Doug Smith, Steven Hardiman, Paul Halloran, Craig MacLachlan, James Camp, Peili Zhang, Mark Stringer, et al. Skilful global seasonal predictions from a machine learning weather model trained on reanalysis data. npj Climate and Atmospheric Science, 8:314, 2025. DOI: 10.1038/s41612-025-01198-3.

[52] Dmitrii Kochkov, Janni Yuval, Ian Langmore, Peter Norgaard, Jamie Smith, Griffin Mooers, Milan Klower, James Lottes, Stephan Rasp, Peter Dueben, Sam Hatfield, Peter Battaglia, Alvaro Sanchez-Gonzalez, Matthew Willson, Michael P. Brenner, and Stephan Hoyer. Neural general circulation models for weather and climate. Nature, 632:1060-1066, 2024. DOI: 10.1038/s41586-024-07744-y.

[53] Ilan Price, Alvaro Sanchez-Gonzalez, Ferran Alet, Tom R. Andersson, Andrew El-Kadi, Dominic Masters, Timo Ewalds, Jacklynn Stott, Shakir Mohamed, Peter Battaglia, Remi Lam, and Matthew Willson. Probabilistic weather forecasting with machine learning. Nature, 637:84-90, 2025. DOI: 10.1038/s41586-024-08252-9.